

# SINBAD: A synchrotron infrared beamline at DAΦNE

G.R. Ambrogini,<sup>1</sup> E. Burattini,<sup>2,3</sup> P. Calvani,<sup>1</sup> A. Marcelli,<sup>3</sup>  
C. Mencuccini,<sup>4</sup> A. Nucara<sup>1</sup> and M. Sánchez del Río<sup>5</sup>

<sup>1</sup>Università La Sapienza, Dipartimento di Fisica, P.le A. Moro 5, 00185 Roma, Italy

<sup>2</sup>Università di Verona, Facoltà di Scienze, 37100 Verona, Italy

<sup>3</sup>I.N.F.N. - Laboratori Nazionali di Frascati, C. P. 13, 00044 Frascati, Italy

<sup>4</sup>Università La Sapienza, Dipartimento di Energetica, P.le A. Moro 5, 00185 Roma, Italy

<sup>5</sup>European Synchrotron Radiation Facility, BP. 220, 38043 Grenoble, France

(Presented on 20 October 1995)

Different optical layouts for a beamline that extracts infrared synchrotron radiation from a bending magnet are discussed, and their performances are compared by use of ray-tracing simulations. Specific results are presented for SINBAD, the beamline to be mounted on the new Frascati collider DAΦNE.

©1996 American Institute of Physics.

## I. INTRODUCTION

We discuss the estimated performances of two different optical layouts for the beamline SINBAD (Synchrotron radiation INfrared Beamline At DAΦNE) that we are projecting for the new high-current collider DAΦNE (Frascati, Italy). Both rings of DAΦNE have a circumference of 97.69 m, an accumulation energy of 0.51 GeV, and eight bending magnets with a radius of 1.4 m. More detailed information is given in Table I and Ref. 1.

SINBAD is designed to work for Fourier transform spectroscopy in the wavelength range from 5 to 5000  $\mu\text{m}$ . However, with a proper choice of mirror coatings, shorter wavelengths could also propagate in the beamline. This latter consists of two parts. The ultrahigh vacuum (UHV) section transmits radiation from a bending magnet of DAΦNE to the diamond window (DW), while the high-vacuum (HV) section connects the DW to the interferometer. While the optics of the former section will be built as described in this report, different optical layouts are under consideration for the high-vacuum part. Two possible optics are here described in more detail. Many others, including a simpler waveguide layout, are still being examined.

The characteristics of the bending magnets of DAΦNE as sources of IRSR have been published elsewhere.<sup>1</sup> The actual brilliance ratio (ABR) between the DAΦNE bending magnet and a black body has been shown to be  $10^3$  at 100  $\mu\text{m}$ .<sup>2</sup> The actual source area<sup>2</sup> (ASA) has been accurately evaluated, in order to get reliable parameters for the ray-tracing simulation of the source. This has been accomplished by use of SHADOW<sup>3</sup> software, which has produced most of the results presented here. The horizontal ( $x$ ) and vertical ( $y$ ) dimensions of the source, as seen by the beamline, are reported in Table I for different wavelengths.

TABLE I. Dimensions of the DAΦNE source, including the diffraction term contribution, at different wavelengths.

( $\mu\text{m}$ )	$x$ (mm)	$y$ (mm)
20	2.12	0.32
50	2.17	0.33
100	2.18	0.35
1000	2.28	0.76

The front-end flange, placed at 1.2 m from the center of the virtual source, limits the clear aperture to 50 mrad, both in the horizontal and in the vertical plane. It does not produce any appreciable effect at  $< 200 \mu\text{m}$ , while it causes a significant reduction of the intensity at longer wavelengths. The optimum collection angle in the horizontal plane has been shown to be 20 mrad,<sup>1,2</sup> value that has been used in all the present simulations.

## II. THE ULTRAHIGH VACUUM SECTION

The optics of the UHV section consist of two mirrors at about 50 cm apart, so that they can be inserted in a unique vessel.<sup>1</sup> The extraction mirror M1 is plane and is placed at 300 cm from the source. It deflects the beam by 90° upwards. The ellipsoidal mirror M2 focuses the beam on the DW. The angle of incidence on M2 is also 45°, so that the beam on the DW is parallel to that which leaves the front end. The parameters and the dimensions of M1 and M2 are listed in Table II. The spatial distribution of the radiation on the DW at 100  $\mu\text{m}$  is shown in Fig. 1. As one can see, a sharply focused image of the source is obtained.

The quality requirements on the reflecting surfaces have also been evaluated. While a satisfactory roughness is easily obtained at infrared wavelengths by standard polishing, the tolerance on the slope of the mirror surface has to be evaluated. We have then generated a surface with a slope error  $= 31 \mu\text{rad}$  in the  $x$  direction (sagittal plane)

TABLE II. Parameters of the two mirrors of the UHV section. Her, m.o. is the orientation angle of the reflecting surface in the coordinate system of SHADOW (see Ref. 3).

	Distance from the source (cm)	Incidence angle	figure	Mirror parameters		m.o. angle
				major semi-axis (cm)	minor semi-axis (cm)	
M1	300	45°	PLANE			0°
M2	350	45°	ELLIPSOIDAL	233.5	143.1	180°

and  $\theta = 19 \mu\text{rad}$  in the  $y$  direction (tangential plane). Ray-tracing simulations show that under these conditions the divergence along  $x$  is unaffected. In turn, a tangential error of  $48 \mu\text{rad}$  increases the divergence along  $y$  even at  $\theta = 1 \mu\text{rad}$  ( $\theta_y \sim 0.040$ ). The effects of an incorrect alignment of the mirrors have been evaluated by purposely introducing small errors in the angle of incidence. The results indicate that a deviation from the ideal condition should be observed only in the vertical direction (tangential plane), for angular errors greater than  $0.2^\circ$ . Small translational displacements of the curved mirrors have also been tested and found to produce only negligible effects on the pattern shown in Fig. 1.

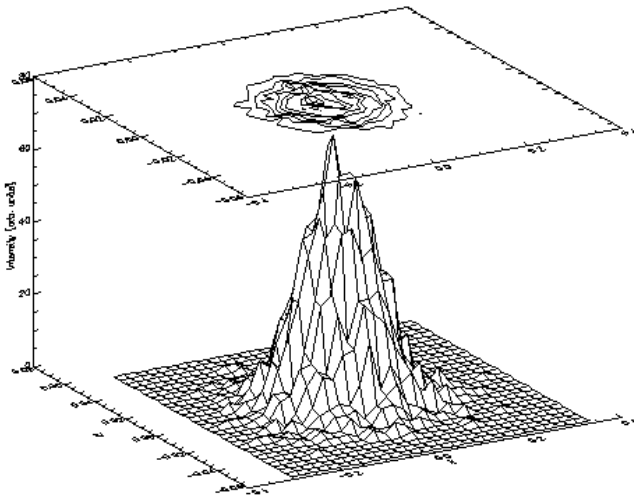


FIG. 1. The intensity distribution of the radiation focused on the diamond window for SINBAD at DA NE. The calculation consider 20 mrad in the horizontal plane and all the vertical divergence allowed by a CF 63 at  $100 \mu\text{m}$ .  $x$  and  $z$  coordinates are in cm.

The power incident on M1 will not be exceedingly high (150 W at an electron current of  $I=1 \text{ A}$ ) due to the low critical energy of the ring working at 0.75 GeV. However, the distortion of M1 caused by thermal load has been evaluated by modeling its surface as a plane in the horizontal dimension and as a convex cylinder of radius  $R$  along the vertical direction. At first order, the expression for the slope associated with the thermal bump is:<sup>4</sup>

$$\theta = \left( \frac{1}{k} \right) \frac{\ell}{2} Q \quad (1)$$

where  $\ell$  is the mirror length and  $Q$  is the incident power. For SINBAD,  $Q=8 \text{ watt/cm}^2$  and  $\ell = 250 \text{ mm}$ . If we consider the extraction mirror made in SiC or Cu for their low thermal expansion/conductivity ratio  $1/k$ ,<sup>5</sup> we obtain

$\theta = 0.32 \text{ mrad}$  for SiC and  $\theta = 0.43 \text{ mrad}$  for Cu. These slopes correspond to  $R=781 \text{ m}$  and  $R=581 \text{ m}$ , respectively. Such deformations are able to increase the spot dimension on the DW at  $\theta = 50 \mu\text{m}$  by nearly a factor of two.

The last optical element of the UHV section is the diamond window. A chemical vapor deposition diamond (CVDD) disk, about  $250 \mu\text{m}$  thick, is being tested. The main advantage of a CVDD window is its lower cost with respect to natural diamond. Wedged CVDD windows, which reduce interference effects, are also available. Alternatively, a flat window can be mounted at the Brewster angle, which for CVDD is  $67.2^\circ$ .

The details of all the calculations reported in this Section can be found in Ref. 5.

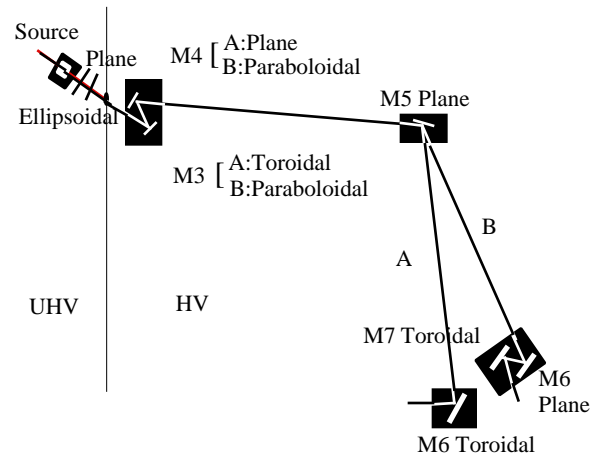


FIG. 2. Layouts of SINBAD, as seen in a horizontal plan, for the two HV sections of beamlines A and B.

### III. THE HIGH-VACUUM SECTION

The second section of the beamline is intended to produce a faithful image of the DW on the entrance pupil of the interferometer. A high vacuum ( $p < 10^{-6} \text{ Torr}$ ) has to be kept in this section, which in the case of SINBAD has to be very long, in order to connect the collider hall with the experimental area outside the shielding wall. We have simulated the behavior of several beamlines,<sup>5</sup> differing from one to other in the number and shape of the mirrors. The best performances were given by the two optical layouts shown in Fig. 2, which will be described in the following.

TABLE III. Parameters of the mirrors for the beamline A.

	distance from DW (cm)	incidence angle	figure	mirror parameters		m.o. angle
				major radius (cm)	minor radius (cm)	
M3	50	15°	TOROIDAL	103.52	96.60	90°
M4	100	32.5°	PLANE			180°
M5	518	75°	PLANE			0°
M6	1285	30°	TOROIDAL	115.47	86.60	90°

TABLE IV. Standard deviations for the images produced by beamline A.  $s_y$  and  $s'_y$  are the width at half maximum of the non-Gaussian distributions.

( $\mu\text{m}$ )	$x$ (cm)	$s_y$ (cm)	$s'_x$ (rad)	$s'_y$ (rad)	$n_{\text{lost}}$ (%)
20	0.07	0.048	0.036	0.097	<1
50	0.07	0.072	0.037	0.136	6
100	0.07	0.072	0.037	0.136	17
1000	0.07	0.053	0.039	0.152	62

**Beamline A.** The first optical layout includes two toroidal mirrors plus two plane mirrors (see the top view of the optical path in Fig. 2). The first toroid, placed at 50 cm from the DW, deflects back the radiation by 30° and collimates the radiation into a plane wave. The second toroid focuses again the radiation on the aperture stop of the interferometer. The total optical path is about 15 m. The mirror parameters are listed in Table III.

The intensity distribution of the image produced by beamline A is shown at a wavelength of 100  $\mu\text{m}$  in Fig. 3 (top). The magnification is one, both in the sagittal and the tangential planes, in order to minimize aberrations. A rough estimate of the magnitude of the line distortion in the present case gives a broadening of 1 mm, i.e., comparable with the size of the observed image (see Table IV).

**Beamline B.** It includes two paraboloidal and a toroidal mirror whose parameters are reported in Table V. The first paraboloid defocuses the beam in the tangential plane; the second one does the same in the sagittal plane. The final toroid refocuses the parallel beam on the interferometer pupil. The optical path is again about 15 m. The image is shown for 100  $\mu\text{m}$  in Fig. 3 (bottom). Ray-tracing data are summarized in Table VI.

In order to determine the size of the mirrors for both beamlines, one should calculate the area of the beam at each reflection. This can be done either by ray-tracing simulation or by simple geometrical considerations.<sup>5</sup> The results are compared in Table VII for beamline A. The aberrations, the diffraction and the different properties of the reflecting surfaces contribute to a residual divergence that accounts for the difference in the data set obtained by ray tracing in Table VII.

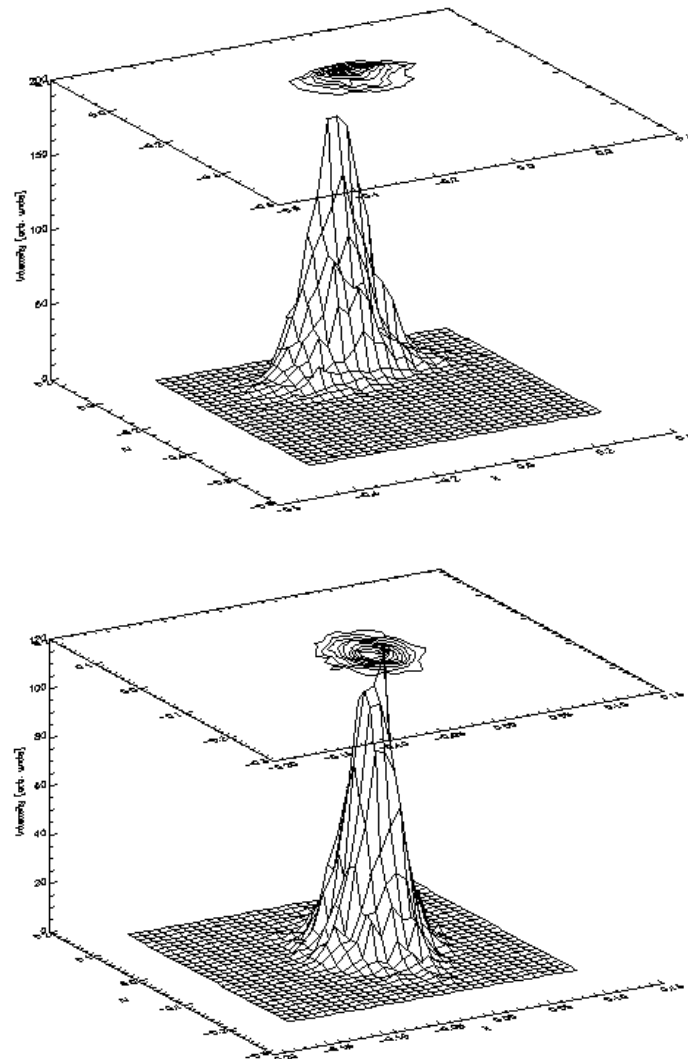


FIG. 3. Intensity distribution of the radiation focused on the pupil of the interferometer, if placed at the end of beamline A (top) or B (bottom).  $x$  and  $y$  coordinates are in cm.

TABLE V. Parameters of the mirrors of beamline B.  $p$  is the parabola parameter.<sup>5</sup>

	distance from the DW (cm)	incidence angle	figure	mirror parameters			m.o. angle
				major radius (cm)	minor radius (cm)	$p$ (cm)	
M3	50	15°	PARABOLOIDAL			93.3	90°
M4	150	28.5°	PARABOLOIDAL			142.26	180°
M5	665	76.5°	PLANE				0°
M6	1180	15°	PLANE				90°
M7	1487.5	15°	TOROIDAL	103.01	96.11	186.6	0°

TABLE VI. Standard deviations for the images produced by beamline B.  $s'_x$  and  $s'_y$  as in Table IV.

( $\mu\text{m}$ )	$x$ (cm)	$y$ (cm)	$s'_x$ (rad)	$s'_y$ (rad)	$n_{\text{lost}}$ (%)
20	0.014	0.035	0.11	0.12	<1
50	0.017	0.036	0.14	0.12	6
100	0.018	0.036	0.14	0.12	17
1000	0.027	0.038	0.14	0.12	63

TABLE VII. The horizontal (H) and vertical (V) dimensions (in cm) of the illuminated area of the mirrors in beamline A at 50  $\mu\text{m}$ . The results of the geometrical calculation are compared with those obtained by SHADOW.

	GEOMETRICAL	RAY TRACING
M1	H= 6, V= 16.5	H=7.5, V= 24
M2	H= 7, V= 19.3	H= 8, V= 24
M3	H= 3.1, V= 5.85	H= 5, V= 8
M4	H= 3.7, V= 5.85	H= 5, V= 8
M5	H= 11.9, V= 5.85	H= 20, V= 8
M6	H= 3.5, V= 5.85	H= 14, V= 9

The optical coupling of the beamline to the Michelson interferometer has also been studied by ray-tracing simulation. Numerical estimates have been done for a BOMEM DA8 spectrophotometer. This latter has a plane mirror, 7.5 cm in diameter, that deviates the beam towards a collimating spherical mirror with  $R=64.8$  cm and  $f/4$  optics. The beam splitter is placed at 25 cm from the collimator. In the simulation, we used a conventional source, like a black body or a Globar, emitting monochromatic radiation at 50, 100 or 1000  $\mu\text{m}$  uniformly, over a cone of 0.16 sterad. Now, one may define the ABR as the ratio between the flux per unit solid angle and unit area received by the beamsplitter when illuminated by a conventional source and the flux (defined in the same way) when illuminated by SINBAD.<sup>5</sup> We define here the brilliance as the flux of photons in the solid angle for a small bandwidth ( $10^{-3}$ ) normalized to the ASA. At the source and for  $\lambda = 50$   $\mu\text{m}$ , one obtains<sup>5</sup> the previously mentioned ideal value of  $10^3$ . At the entrance of the interferometer, the ABR is reduced to 58 for beamline A and to 74 for B. The advantage of the SR source with respect to a

blackbody is still considerable, even if both optics reduce the ABR by more than one order of magnitude.

The instrumental resolution of the interferometer is clearly limited by the beam divergence and by the spot size. Accurate calculations of these effects have been already performed.<sup>6,7</sup> By using a simpler model,<sup>5</sup> which however gives results in very good agreement with the above estimates, we found the standard deviation of the angular distribution, after the collimator of the interferometer, to be about  $0.15 \times 10^{-2}$  rad both in the horizontal and the vertical dimensions and for both layouts A and B. This gives an intrinsic divergence  $= 2.25 \times 10^{-6}$  rad<sup>2</sup> and a maximum instrumental resolution of  $0.126 \text{ cm}^{-1}$  at  $\lambda = 50$   $\mu\text{m}$ .

## ACKNOWLEDGMENTS

The authors wish to thank G. P. Williams, H. Buys, G. Cappuccio, A. Grilli, A. Raco and S. Simeoni for useful discussions and suggestions. This work has been supported in part by the Human Capital & Mobility Programme of the European Union (Contract CT94-0551).

- 1 E. Burattini, G. Cappuccio, A. Marcelli, P. Calvani, A. Nucara, and M. Sánchez del Río, Nucl. Instr. Meth. A **347**, 308 (1994).
- 2 A. Nucara, G.R. Ambrogini, P. Calvani, A. Marcelli, and M. Sánchez del Río, Rev. Sci. Instr. **66**, 1934 (1995), and LNF Report 94/053 (IR) 1994.
- 3 C. Welna, G.J. Chen, and F. Cerrina, Nucl. Instr. Meth. A **347**, 344 (1994).
- 4 R.K. Smither, Nucl. Instr. Meth. A **291**, 286 (1990).
- 5 G.R. Ambrogini, E. Burattini, P. Calvani, A. Marcelli, A. Nucara, and M. Sánchez del Río, to be published.
- 6 W.D. Duncan and G.P. Williams, Appl. Opt. **22**, 2914 (1983).
- 7 B. Nelander, Vibrational Spectroscopy **9**, 29 (1995).